Computer Modeling in Engineering & Sciences

Tech Science Press

https://doi.org/10.32604/cmes.2026.091601

ARTICLE

A Grid-Aware Agent-Based Computational Framework for Renewable-Generation Capacity Allocation in Transmission Networks

Shenglei Du[1], Qinjuan Wang[2], Zhuxiu Wang[2], Yalu Sun[2] and Zhaobin Li[3,*]

[1]College of Information Science and Engineering, Lanzhou University, Lanzhou, China
[2]Economic and Technological Research Institute, State Grid Gansu Electric Power Company, Lanzhou, China
[3]College of Artificial Intelligence and Computer Science, Northwest Normal University, Lanzhou, China

*Corresponding Author: Zhaobin Li. Email: zhaobinli@nwnu.edu.cn

Received: 24 August 2026; Accepted: 20 October 2026; Published: 17 November 2026

ABSTRACT: Renewable-generation capacity allocation in transmission networks requires joint consideration of heterogeneous generation profiles, nodal load characteristics, and network constraints. A complementary modeling need is to make the interaction between local capacity adaptation and evolving grid feedback observable during allocation formation. This study develops a grid-aware agent-based computational framework that represents planned generation-capacity increments as adaptive agents interacting within a shared transmission-network environment. Candidate nodes are evaluated using non-hydro renewable accommodation, temporal resource–load matching, and constraint-related information associated with capacity, ramping, and transmission-section limits. Accepted migration and cooperation actions modify nodal injections and network states, allowing subsequent agent decisions to respond to the evolving grid environment. The framework is evaluated on an anonymized provincial 330/750 kV transmission network using chronological annual profiles at hourly resolution. Across 10 independent runs, the proposed framework achieves a mean annual non-hydro renewable accommodation of 16.0083 million MWh, representing a 1.46% improvement over the original allocation and a 0.71% improvement over a particle swarm optimization benchmark, while reaching 98.7% of a centralized mixed-integer linear programming benchmark under the same direct-current power-flow formulation. The corresponding curtailment rate increases from 13.33% to 14.37%, revealing an accommodation–congestion trade-off as capacity reallocation improves renewable utilization while increasing exposure to binding transmission sections. The results establish an interpretable connection between local capacity adaptation, grid feedback, and system-level allocation outcomes, providing a planning-level basis for coordinating generation-capacity allocation with transmission capability.

KEYWORDS: Agent-based modeling; renewable-generation capacity allocation; transmission networks; renewable accommodation; transmission congestion

1 Introduction

The increasing penetration of variable renewable generation is reshaping long-term power-system planning. Wind and photovoltaic (PV) resources exhibit pronounced temporal variability, and the growing diversity of generation technologies makes the system-level value of new capacity increasingly dependent on temporal complementarity among resources. Recent planning studies emphasize the importance of preserving chronological renewable-generation characteristics, and large-scale evidence indicates that wind–solar complementarity can increase effective renewable penetration by mitigating temporal imbalance [1,2]. Generation planning therefore involves both the amount of capacity to be added and its spatial

Copyright © 2026 The Authors. Published by Tech Science Press. This work is licensed under a Creative Commons Attribution 4.0 International License, which permits unrestricted use, distribution, and reproduction in any medium, provided the original work is properly cited.

distribution across the network, since different nodal allocations lead to different resource-utilization and operating conditions.

This allocation problem is intrinsically coupled with nodal load characteristics, resource availability, and network capability. Wind, PV, hydropower, thermal power, and concentrating solar power (CSP) exhibit distinct output and regulation characteristics, and load profiles vary across nodes and time periods. Allocation quality therefore depends on local resource potential, temporal compatibility between generation and demand, and network transfer capability. Recent studies show substantial temporal and spatial heterogeneity in renewable complementarity and source–load matching, while long-term mismatches between renewable production and demand can require additional intertemporal flexibility [3,4]. Co-planning studies further demonstrate that siting and sizing decisions materially affect renewable hosting capability and network operating efficiency [5]. Generation-capacity allocation is therefore a coupled spatiotemporal and network-constrained planning problem.

Centralized mathematical optimization provides a rigorous foundation for addressing such planning problems. By explicitly defining objectives, decision variables, uncertainty sets, and network constraints, optimization-based formulations can identify system-level allocations that satisfy prescribed technical requirements. Recent studies have characterized security boundaries for renewable generation and developed distributionally robust formulations for wind and PV uncertainty under network constraints [6,7]. Decision-oriented modeling also emphasizes the coupling between renewable information and downstream system decisions [8]. These developments establish a strong basis for determining system-level planning solutions. A complementary modeling question concerns how individual planned capacity increments adapt to local resource–load conditions and evolving network feedback during allocation formation.

A computational representation of local adaptation makes the allocation-formation process observable at the decision level. A local reassignment changes nodal injections and network loading, and the updated network state subsequently alters the attractiveness or feasibility of candidate decisions. Repeated local interactions thereby produce a system-level allocation through successive state transitions. Agent-based and decentralized energy-system studies have shown that explicit representation of local decision entities and network congestion can reveal this decision–feedback interaction [9]. This representation is particularly relevant when the analytical focus includes both the final allocation and the trajectory through which accommodation and congestion patterns emerge.

Motivated by this need, this study investigates the nodal allocation of heterogeneous planned generation-capacity increments under fixed total capacity plans. The planning objective is to maximize annual non-hydro renewable accommodation for wind, PV, and CSP generation subject to capacity, ramping, and transmission-section constraints under a direct-current power-flow (DCPF) model. The proposed agent-based model (ABM) represents planned generation-capacity increments as adaptive agents interacting within a shared transmission-network environment. Each local evaluation combines resource–load compatibility with constraint-related feedback, and accepted reassignments update the network state used by subsequent decisions. The framework provides a planning-level computational representation of allocation evolution alongside centralized system-level optimization.

The main contributions of this study are summarized as follows.

- **Agent–grid feedback representation for generation-capacity allocation.** A grid-aware agent-based computational representation is established in which planned generation-capacity increments act as adaptive agents and the transmission network serves as a shared environment. Local migration and cooperation modify nodal injections and network states, while capacity, ramping, and transmission-section information is returned to subsequent agent evaluation and feasibility screening.

This closed-loop representation makes the interaction between local capacity reassignment and grid feedback explicit during allocation evolution.

- **Node-aware temporal resource–load matching for local allocation decisions.** A node-aware feature representation is developed to transform the temporal characteristics of generation output and nodal load into a local matching signal for candidate-node evaluation. The resulting agent-level decision rule combines non-hydro renewable accommodation, temporal resource–load compatibility, and constraint-violation penalties, thereby linking temporal complementarity with network-constrained local capacity reassignment and enriching candidate-node evaluation with information beyond resource potential.
- **Interpretable linkage between local adaptation and system-level accommodation and congestion.** The framework makes it possible to trace how repeated local evaluation, migration, cooperation, and grid feedback collectively shape the resulting capacity allocation. This establishes an observable connection from agent-level adaptation to system-level non-hydro renewable accommodation and transmission congestion, providing a planning-oriented basis for diagnosing how allocation changes create both accommodation gains and congestion-sensitive conditions.

The remainder of this paper is organized as follows. Section 2 reviews renewable-generation planning, interaction-oriented energy methods, and artificial intelligence and heuristic methods for power systems, and clarifies the research gap addressed in this study. Section 3 formulates the generation-capacity allocation problem, performance metrics, system-level objective, network constraints, and modeling scope. Section 4 presents the grid-aware agent-based computational framework, including agent and environment definitions, resource models, node-aware feature representation, agent-level fitness, interaction rules, and convergence procedure. Section 5 reports the case study and experimental results. Section 6 discusses the mechanisms underlying local adaptation, the accommodation–congestion trade-off, and the modeling boundary and engineering implications. Section 7 concludes the paper.

2 Related Work

2.1 Renewable Generation Planning and Allocation

Renewable-generation planning increasingly couples capacity decisions with grid development, spatial allocation, and flexible demand. Recent studies have reviewed optimization strategies for distributed-generation sizing and allocation, formulated joint generation–transmission expansion planning with heterogeneous demand-side resources, and shown that explicitly representing grid development can materially change capacity-expansion outcomes [10–12]. These studies demonstrate the maturity of centralized mathematical programming for determining technically and economically feasible system-level planning solutions. Their primary outputs are typically installed capacities, siting decisions, transmission investments, or other system-level planning variables.

As renewable penetration increases, planning formulations have incorporated a wider range of uncertainty, resilience, flexibility, and security requirements. Two-stage robust and resilience-oriented models account for uncertain equipment contingencies and decision-dependent uncertainties in integrated energy systems [13,14]. Other recent formulations introduce intertemporal hydrogen-storage flexibility and multiple uncertainty sources, or explicitly impose system-strength requirements when planning grid-forming energy storage in renewable-rich systems [15,16]. Such developments improve the physical realism and robustness of planning decisions, but they remain predominantly system-level optimization formulations in which a prescribed objective and constraint set determine a preferred planning solution.

Spatial configuration constitutes another important dimension of renewable-generation planning. Recent studies optimize offshore-wind collector-system layouts under post-fault network reconfiguration, jointly determine offshore wind-farm layouts and electrolyzer capacities, and address wind-turbine micro-siting through hybrid optimization [17–19]. Although these problems operate at spatial scales different from transmission-network nodal allocation, the reported results show that the location of generation-related assets can materially affect energy yield, reliability, infrastructure requirements, and downstream operating conditions. The studies also illustrate that spatial decisions are commonly formulated as siting, sizing, or layout variables within centralized optimization models.

Network capability further constrains the benefits attainable from renewable deployment. Recent work has examined phase-shifting-transformer sizing for congestion management in renewable-rich regions and reviewed methods for improving renewable hosting capacity under power-quality and network limitations [20,21]. Long-horizon renewable planning can also be influenced by technology- and environment-dependent effects; for example, projected temperature changes can alter photovoltaic degradation, lifetime, and cost [22]. Taken together, the planning literature increasingly integrates spatial, temporal, network, uncertainty, and reliability considerations. These formulations primarily characterize system-level planning outcomes, leaving the evolution of individual planned capacity increments among candidate nodes as a complementary modeling dimension.

2.2 Game-Theoretic, Multi-Agent, and Agent-Based Energy Methods

Interaction-centered methods provide a complementary perspective by explicitly representing decisions and coordination among multiple entities. Cooperative multi-agent energy-system operation has been formulated through asymmetric Nash bargaining, while holonic smart-grid architectures organize decision making among interacting autonomous units [23,24]. Agent-based modeling has also been used to simulate long-term renewable power-system evolution by representing power generators, policymakers, and consumers as interacting decision entities, thereby linking heterogeneous micro-level decisions with aggregate system evolution [25]. Such formulations are particularly useful when negotiation, cooperation, information exchange, or distributed decision structures are central to the problem. Compared with a single system-level optimization variable set, they make the roles and interactions of individual decision entities more explicit and therefore provide a natural basis for studying collective behavior in complex energy systems.

Recent learning-based multi-agent studies further strengthen this adaptive perspective. Adaptive multi-agent reinforcement learning has been used to coordinate flexible resources in virtual power plants with dynamically participating buildings. Learning-based coordination has also been applied to community-microgrid co-scheduling, while distributed attention-enabled multi-agent reinforcement learning has been developed for power-system frequency regulation [26–28]. These approaches allow local or distributed decisions to respond to changing system states and coordination signals, demonstrating the role of repeated interaction in adaptive operation of renewable-rich energy systems.

Recent agent-oriented studies mainly associate agents with operational entities, controllers, market participants, or flexible resources, with decisions centered on scheduling, regulation, cooperation, or energy sharing. The planning question considered here assigns agency to discrete planned generation-capacity increments and follows their virtual reassignment among candidate transmission-network nodes as each accepted decision updates the grid state. This perspective places the allocation trajectory and its interaction with network constraints at the center of analysis.

2.3 Artificial Intelligence and Heuristic Methods for Power Systems

Artificial intelligence and heuristic methods have expanded the available tools for high-dimensional and adaptive power-system decision problems. Hybrid expert-knowledge and reinforcement-learning methods have been developed for real-time scheduling of renewable-rich power systems [29]. Model-based safe reinforcement learning further demonstrates how learned decision policies can be coupled with feasibility requirements in active distribution-network scheduling [30]. These developments highlight the potential of learning-based methods to support adaptive decision making in complex power-system environments under time-varying operating conditions and feasibility constraints.

Learning-based methods have also been applied to a broad range of operational and state-awareness tasks. Deep reinforcement learning has been used for active-network management and emergency load shedding, while brain-inspired reinforcement learning has been developed for load-frequency control under composite disturbances [31,32]. Their common advantage is the ability to extract adaptive decision or estimation policies from changing system states, thereby complementing conventional analytical and optimization-based approaches in complex operating environments.

Data-driven methods are increasingly combined with explicit physical and safety constraints. Neural-network-based stability constraints can be embedded into power-system dispatch optimization, while safe data-driven smart-grid frameworks provide structured environments for constrained learning and control [33,34]. Model-based adaptive optimization also remains important; look-ahead rolling economic dispatch can explicitly coordinate generation ramping capability and flexible load transfer in renewable-integrated systems [35]. These studies establish mature tools for adaptive control, estimation, scheduling, constrained learning, and intelligent search. The present planning problem focuses on a different decision object: the progressive formation of a nodal generation-capacity allocation through successive local capacity reassignments.

2.4 Research Gap and Position of this Work

Recent reviews cover low-carbon power-system planning, renewable-generation capacity planning under high renewable penetration, and game-theoretic methods for new power systems [36–38]. Collectively, these studies address planning, reliability, uncertainty, strategic interaction, and adaptive decision making through complementary methodological frameworks. Centralized optimization determines system-level planning decisions under explicit objectives and constraints. Interaction-oriented methods expose coordination among multiple entities, while learning and heuristic methods provide adaptive search and control mechanisms for complex power-system environments.

Across the reviewed literature streams, three modeling opportunities emerge when allocation evolution is treated as an explicit object of analysis. First, representing individual planned capacity increments as local decision entities makes the formation of a system-level allocation observable. Second, temporal resource–load complementarity and network-constraint feedback can be incorporated directly into repeated local candidate evaluations. Third, tracing these local decisions provides a direct link between adaptation trajectories and system-level renewable accommodation and congestion formation. These opportunities motivate the computational representation developed in this study.

Accordingly, this study uses agent-based modeling as a planning-level representation of capacity-allocation evolution. Planned heterogeneous generation-capacity increments act as adaptive agents within a shared transmission-network environment, allowing local evaluation and reassignment to interact with network feedback. The framework links local resource adaptation with system-level non-hydro renewable accommodation and transmission congestion under the adopted planning constraints.

3 System Model and Problem Formulation

3.1 Problem Setting and Performance Metrics

A grid-constrained nodal generation-capacity allocation problem is considered for a power system with heterogeneous generation resources, nodal loads, and transmission-section limits. Let $\mathcal{N} = \{1, 2, \ldots, M\}$ denote the node set, $\mathcal{T} = \{1, 2, \ldots, N_t\}$ denote the hourly time set, and $\mathcal{G}$ denote the generation-type set. The set of discrete planned generation-capacity blocks is denoted by $\mathcal{K}$. Each capacity block $k \in \mathcal{K}$ has a fixed capacity c_k and belongs to one generation type $g(k) \in \mathcal{G}$. Let $\mathcal{K}_g = \{k \in \mathcal{K} \mid g(k) = g\}$ denote the subset associated with generation type g.

The subset of non-hydro renewable-generation capacity blocks is denoted by $\mathcal{K}_{\mathrm{NHR}}$ and includes wind power, PV power, and CSP. Hydropower and thermal power are modeled as dispatchable resources, and their capacity-block set is denoted by $\mathcal{K}_{\mathrm{D}}$. CSP remains part of $\mathcal{K}_{\mathrm{NHR}}$ for renewable-generation accounting, while its thermal-storage flexibility is represented separately in the ramping constraints. Let $z_{k,m} \in \{0, 1\}$ indicate whether capacity block k is allocated to node m.

For generation type g, the capacity allocated to node m under assignment $\mathbf{z}$ is

$$C_{g,m}^{\mathrm{alloc}} = \sum_{k \in \mathcal{K}_g} c_k z_{k,m}, \qquad g \in \mathcal{G},\ m \in \mathcal{N}. \tag{1}$$

The annual non-hydro renewable accommodation is defined as

$$E_{\mathrm{acc}} = \sum_{t \in \mathcal{T}} \sum_{m \in \mathcal{N}} \sum_{k \in \mathcal{K}_{\mathrm{NHR}}} P_{k,m,t}^{\mathrm{acc}} \Delta t, \tag{2}$$

where $P_{k,m,t}^{\mathrm{acc}}$ denotes the accommodated active-power output of non-hydro renewable capacity block k at node m and time t. The assignment-dependent output bounds introduced below ensure that $P_{k,m,t}^{\mathrm{acc}} = 0$ when capacity block k is not allocated to node m. The time-step length is denoted by Δt, with $\Delta t = 1$ h for the hourly profiles used in the case study.

The annual non-hydro renewable curtailment is defined as

$$E_{\mathrm{cur}} = \sum_{t \in \mathcal{T}} \sum_{m \in \mathcal{N}} \sum_{k \in \mathcal{K}_{\mathrm{NHR}}} \left(z_{k,m} P_{k,m,t}^{\mathrm{ava}} - P_{k,m,t}^{\mathrm{acc}} \right) \Delta t, \tag{3}$$

where $P_{k,m,t}^{\mathrm{ava}}$ denotes the available output of capacity block k at node m before curtailment. The corresponding annual non-hydro renewable curtailment rate is

$$r_{\mathrm{cur}} = \frac{E_{\mathrm{cur}}}{E_{\mathrm{acc}} + E_{\mathrm{cur}}}. \tag{4}$$

The accommodation, curtailment, and curtailment rate characterize the renewable-generation utilization associated with a capacity allocation. Annual accommodation constitutes the system-level planning objective, whereas curtailment and curtailment rate are retained as performance indicators for evaluating the utilization and congestion consequences of the resulting allocation.

3.2 System-Level Objective

The planning problem determines the nodal allocation of the prescribed generation-capacity blocks to maximize annual non-hydro renewable accommodation subject to capacity-allocation, generation-output,

active-power balance, ramping, and transmission-section feasibility conditions. The system-level problem is formulated as

$$\begin{aligned} \mathcal{P}: \quad & \max_{\mathbf{z},\mathbf{P}^{\mathrm{acc}},\mathbf{P}^{\mathrm{disp}},\mathbf{w},\boldsymbol{\theta},\mathbf{f}} \quad E_{\mathrm{acc}} \\ & \text{s.t.} \quad (6)-(15). \end{aligned} \tag{5}$$

The aggregate planned capacity of each generation type is prescribed. Accordingly, $\mathcal{P}$ determines the spatial distribution of the fixed capacity portfolio. The binary vector $\mathbf{z}$ contains the primary nodal allocation decisions, while $\mathbf{P}^{\mathrm{acc}}$, $\mathbf{P}^{\mathrm{disp}}$, $\mathbf{w}$, $\boldsymbol{\theta}$, and $\mathbf{f}$ characterize the corresponding active-power feasibility state.

3.3 Network and Planning Constraints

Each generation-capacity block is assigned to exactly one candidate node:

$$\sum_{m\in\mathcal{N}} z_{k,m} = 1, \quad k \in \mathcal{K}, \qquad z_{k,m} \in \{0,1\}, \quad k \in \mathcal{K},\ m \in \mathcal{N}. \tag{6}$$

For each generation type, the nodal allocation must preserve the prescribed total capacity:

$$\sum_{m\in\mathcal{N}} C_{g,m}^{\mathrm{alloc}} = C_g^{\mathrm{plan}}, \qquad g \in \mathcal{G}, \tag{7}$$

where $C_g^{\mathrm{plan}} = \sum_{k\in\mathcal{K}_g} c_k$ denotes the fixed total planned capacity of generation type g.

The capacity assigned to an individual node is limited by its admissible planning allocation:

$$0 \le C_{g,m}^{\mathrm{alloc}} \le \overline{C}_{g,m}, \qquad g \in \mathcal{G},\ m \in \mathcal{N}, \tag{8}$$

where $\overline{C}_{g,m}$ denotes the admissible nodal allocation limit for generation type g at node m under the adopted planning setting.

The generation-output variables are coupled with the allocation decisions through

$$\begin{aligned} & 0 \le P_{k,m,t}^{\mathrm{acc}} \le z_{k,m} P_{k,m,t}^{\mathrm{ava}}, \quad k \in \mathcal{K}_{\mathrm{NHR}}, \\ & z_{k,m}\underline{P}_{k,m,t}^{\mathrm{disp}} \le P_{k,m,t}^{\mathrm{disp}} \le z_{k,m}\overline{P}_{k,m,t}^{\mathrm{disp}}, \quad k \in \mathcal{K}_{\mathrm{D}}, \end{aligned} \qquad m \in \mathcal{N},\ t \in \mathcal{T}, \tag{9}$$

where $\underline{P}_{k,m,t}^{\mathrm{disp}}$ and $\overline{P}_{k,m,t}^{\mathrm{disp}}$ denote the aggregate lower and upper active-power output bounds of the corresponding dispatchable resource.

Let $L_{m,t}$ denote the active-power demand at node m and time t. The nodal net active-power injection is

$$w_{m,t} = \sum_{k\in\mathcal{K}_{\mathrm{NHR}}} P_{k,m,t}^{\mathrm{acc}} + \sum_{k\in\mathcal{K}_{\mathrm{D}}} P_{k,m,t}^{\mathrm{disp}} - L_{m,t}, \qquad m \in \mathcal{N},\ t \in \mathcal{T}. \tag{10}$$

The active-power network state is represented by the DCPF model:

$$\begin{aligned} & \mathbf{w}_t = \mathbf{B}\boldsymbol{\theta}_t, \qquad \mathbf{f}_t = \mathbf{H}\mathbf{w}_t, \\ & \sum_{m\in\mathcal{N}} w_{m,t} = 0, \qquad \theta_{m_0,t} = 0, \end{aligned} \qquad t \in \mathcal{T}, \tag{11}$$

where $\mathbf{w}_t$ is the nodal active-power injection vector, $\mathbf{B}$ is the nodal susceptance matrix, and $\boldsymbol{\theta}_t$ is the nodal phase-angle vector. The vector $\mathbf{f}_t$ denotes branch active-power flows, $\mathbf{H}$ is the injection-to-line-flow transfer matrix, and m_0 denotes the reference node.

The residual nodal demand after non-hydro renewable accommodation is defined as

$$R_{m,t} = L_{m,t} - \sum_{k \in \mathcal{K}_{\mathrm{NHR}}} P^{\mathrm{acc}}_{k,m,t}, \qquad m \in \mathcal{N},\ t \in \mathcal{T}. \tag{12}$$

The upward and downward ramping requirements between consecutive hourly states are

$$\begin{aligned} \Delta W^{t}_{m,\mathrm{up}} &= \max\left\{R_{m,t+1} - R_{m,t}, 0\right\}, \\ \Delta W^{t}_{m,\mathrm{down}} &= \max\left\{R_{m,t} - R_{m,t+1}, 0\right\}, \end{aligned} \qquad m \in \mathcal{N},\ t = 1, \ldots, N_t - 1. \tag{13}$$

The required ramping powers must remain within the aggregate regulation capability provided by thermal power, hydropower, and CSP:

$$\begin{aligned} \Delta W^{t}_{m,\mathrm{up}} &\le W^{t,\mathrm{up,max}}_{m,\mathrm{tp}} + W^{t,\mathrm{up,max}}_{m,\mathrm{hyd}} + W^{t,\mathrm{up,max}}_{m,\mathrm{csp}}, \\ \Delta W^{t}_{m,\mathrm{down}} &\le W^{t,\mathrm{down,max}}_{m,\mathrm{tp}} + W^{t,\mathrm{down,max}}_{m,\mathrm{hyd}} + W^{t,\mathrm{down,max}}_{m,\mathrm{csp}}, \end{aligned} \qquad m \in \mathcal{N},\ t = 1, \ldots, N_t - 1. \tag{14}$$

here, $W^{t,\mathrm{up,max}}_{m,\cdot}$ and $W^{t,\mathrm{down,max}}_{m,\cdot}$ denote the available upward and downward regulation capacities of the corresponding flexible generation resources. CSP contributes to these regulation terms through its thermal-storage flexibility while remaining part of non-hydro renewable generation for accommodation accounting.

Let $\mathcal{Q}$ denote the set of monitored transmission sections and $\mathcal{L}_q$ denote the set of branches belonging to section q. Following the adopted section-loading representation, the active-power loading of each monitored section satisfies

$$\sum_{\ell \in \mathcal{L}_q} |f_{\ell,t}| \le F^{\max}_q, \qquad q \in \mathcal{Q},\ t \in \mathcal{T}, \tag{15}$$

where $f_{\ell,t}$ is the active-power flow of branch ℓ and $F^{\max}_q$ is the admissible active-power limit of transmission section q.

3.4 Computational Modeling Scope

The formulation targets planning-level active-power capacity allocation. The aggregate capacity of each generation type is prescribed, and the decision concerns the nodal distribution of discrete planned capacity blocks. Renewable-generation utilization is evaluated using annual hourly profiles, and active-power feasibility is represented through nodal allocation limits, generation-output bounds, power balance, ramping capability, and transmission-section constraints.

The nodal limits $\overline{C}_{g,m}$ represent admissible planning-allocation limits under the adopted active-power formulation. The DCPF model captures the active-power transfer consequences of capacity reallocation. Detailed alternating-current (AC) assessment extends the network representation to reactive-power flow, voltage-magnitude constraints, network losses, and security characteristics. Unit-commitment and investment modules further extend the formulation toward operational and economic planning. Dispatchable resources are represented here through aggregate output and ramping-capability bounds. The resulting formulation provides a strategic planning model for examining the interaction among spatial capacity allocation, temporal resource–load characteristics, non-hydro renewable accommodation, and transmission congestion.

4 Grid-Aware Agent-Based Computational Framework

4.1 Agent and Environment Definition

The framework represents each planned generation-capacity block $k \in \mathcal{K}$ as an adaptive agent interacting with a shared transmission-network environment. An agent is characterized by its generation type $g(k)$, fixed capacity c_k, and current allocated node. The first two attributes remain unchanged during allocation evolution, whereas the node assignment constitutes the principal dynamic state. For iteration n, the state of agent k is represented as

$$\mathbf{s}_k^{(n)} = \left[g(k), c_k, m_k^{(n)} \right], \tag{16}$$

where $m_k^{(n)} \in \mathcal{N}$ denotes the node occupied by agent k at iteration n. The corresponding binary assignment satisfies $z_{k,m}^{(n)} = 1$ when $m = m_k^{(n)}$ and $z_{k,m}^{(n)} = 0$ otherwise.

The shared environment contains the allocation-induced network quantities that are relevant to subsequent local decisions. Its iteration-dependent state is represented by

$$\mathcal{E}^{(n)} = \left\{ \mathbf{C}^{\mathrm{alloc},(n)}, \mathbf{w}^{(n)}, \mathbf{f}^{(n)}, \mathbf{R}^{(n)} \right\}, \tag{17}$$

where $\mathbf{C}^{\mathrm{alloc},(n)}$ denotes the nodal generation-capacity allocation, $\mathbf{w}^{(n)}$ denotes the nodal active-power injections, $\mathbf{f}^{(n)}$ denotes the transmission-line flows, and $\mathbf{R}^{(n)}$ denotes the residual-demand state. The capacity, ramping, and transmission-section limits are fixed environment parameters against which candidate allocations are evaluated.

Allocation evolution is generated through repeated local evaluation and state transition. A candidate action changes one or more agent-node assignments, and an accepted action immediately refreshes the shared environment before subsequent local evaluations are performed. A centralized scheduler coordinates agent evaluation and environment updating, while the allocation trajectory is generated by agent-level local decision rules and feedback-driven state transitions.

4.2 Agent Output Models

The resource layer combines marginal statistical characterization with chronological hourly simulation. Wind-speed and solar-irradiance distributions characterize the statistical variability of renewable resources, while node-specific chronological hourly sequences provide the time-ordered inputs used to construct annual generation profiles. The resulting resource-specific output profiles are used for temporal-feature construction, renewable accommodation evaluation, and grid-feasibility assessment.

For wind power, wind-speed variability is represented by a two-parameter Weibull distribution [39]:

$$f_v(v) = \frac{\beta}{\alpha} \left(\frac{v}{\alpha} \right)^{\beta-1} \exp\left[-\left(\frac{v}{\alpha} \right)^{\beta} \right], \tag{18}$$

where v denotes wind speed, and α and β are the scale and shape parameters, respectively. Let $v_{m,t}$ denote the chronological wind speed at candidate node m and hour t. For a wind agent k with fixed capacity c_k, the available active-power output is calculated using the piecewise turbine power curve [40]:

$$P_{k,m,t}^{\mathrm{ava}} = \begin{cases} 0, & v_{m,t} \le v_{\mathrm{cin}} \text{ or } v_{m,t} > v_{\mathrm{cout}}, \\ \dfrac{v_{m,t} - v_{\mathrm{cin}}}{v_{\mathrm{S}} - v_{\mathrm{cin}}} c_k, & v_{\mathrm{cin}} < v_{m,t} \le v_{\mathrm{S}}, \\ c_k, & v_{\mathrm{S}} < v_{m,t} \le v_{\mathrm{cout}}, \end{cases} \tag{19}$$

where v_{cin}, v_{cout}, and v_{S} denote the cut-in, cut-out, and rated wind speeds, respectively. The sequence $\{P_{k,m,t}^{\mathrm{ava}}\}_{t\in\mathcal{T}}$ forms the chronological available-output profile of the wind agent at candidate node m.

For PV power, normalized solar irradiance is represented by a Beta distribution [41,42]:

$$f_x(x) = \frac{\Gamma(a+b)}{\Gamma(a)\Gamma(b)} x^{a-1}(1-x)^{b-1}, \qquad 0 < x < 1, \tag{20}$$

where x denotes normalized solar irradiance, a and b are positive shape parameters, and $\Gamma(\cdot)$ is the gamma function. Let $x_{m,t}$ denote the normalized chronological irradiance at candidate node m and hour t. For a PV agent k, the corresponding available active-power output is

$$P_{k,m,t}^{\mathrm{ava}} = \begin{cases} c_k, & x_{m,t} > x_{\mathrm{S}}, \\ c_k \dfrac{x_{m,t}}{x_{\mathrm{S}}}, & x_{m,t} \le x_{\mathrm{S}}, \end{cases} \tag{21}$$

where x_{S} denotes the rated normalized irradiance level. The resulting sequence $\{P_{k,m,t}^{\mathrm{ava}}\}_{t\in\mathcal{T}}$ represents the chronological available PV-generation profile at candidate node m.

Hydropower and thermal-power agents are represented by dispatchable output ranges and intertemporal ramping capabilities. Following standard dispatch formulations with ramping limits [43], the operating capability of a hydropower agent is represented as

$$\begin{cases} \underline{P}_{\mathrm{hyd},k} \le P_{\mathrm{hyd},k,t} \le \overline{P}_{\mathrm{hyd},k}, \\ 0 \le \Delta P_{\mathrm{hyd},k,t}^{\mathrm{up}} \le R_{\mathrm{hyd},k}^{\mathrm{up}}, \\ 0 \le \Delta P_{\mathrm{hyd},k,t}^{\mathrm{down}} \le R_{\mathrm{hyd},k}^{\mathrm{down}}, \end{cases} \tag{22}$$

where $\underline{P}_{\mathrm{hyd},k}$ and $\overline{P}_{\mathrm{hyd},k}$ denote the lower and upper output bounds, and $R_{\mathrm{hyd},k}^{\mathrm{up}}$ and $R_{\mathrm{hyd},k}^{\mathrm{down}}$ denote the available upward and downward ramping capabilities. The thermal-power capability is represented as

$$\begin{cases} \underline{P}_{\mathrm{tp},k} \le P_{\mathrm{tp},k,t} \le \overline{P}_{\mathrm{tp},k}, \\ 0 \le \Delta P_{\mathrm{tp},k,t}^{\mathrm{up}} \le R_{\mathrm{tp},k}^{\mathrm{up}}, \\ 0 \le \Delta P_{\mathrm{tp},k,t}^{\mathrm{down}} \le R_{\mathrm{tp},k}^{\mathrm{down}}. \end{cases} \tag{23}$$

here, $\Delta P_{\cdot,k,t}^{\mathrm{up}}$ and $\Delta P_{\cdot,k,t}^{\mathrm{down}}$ denote the upward and downward changes in agent output between adjacent hourly states. The corresponding output ranges and ramping capabilities form the dispatchable flexibility available to the grid during capacity-allocation evaluation.

CSP is represented by a solar-driven generation profile coupled with thermal-energy-storage flexibility. A reduced-order representation is adopted to map chronological solar-resource inputs to electrical output for power-system-level analysis [44]. Let $x_{m,t}^{\mathrm{csp}}$ denote the normalized chronological solar-resource input at candidate node m and hour t. For a CSP agent k, the available active-power output is represented as

$$P_{k,m,t}^{\mathrm{ava}} = \begin{cases} \lambda_{\mathrm{p,e}} c_k, & x_{m,t}^{\mathrm{csp}} > x_{\mathrm{S}}, \\ \lambda_{\mathrm{p,e}} c_k \dfrac{x_{m,t}^{\mathrm{csp}}}{x_{\mathrm{S}}}, & x_{m,t}^{\mathrm{csp}} \le x_{\mathrm{S}}, \end{cases} \tag{24}$$

where $\lambda_{\mathrm{p,e}}$ denotes the aggregate solar-to-electric conversion coefficient. The resulting chronological solar-driven output contributes to non-hydro renewable generation, while the thermal-energy-storage subsystem provides intertemporal regulation capability.

The charging and discharging powers of the thermal-energy-storage subsystem satisfy [44,45]

$$\begin{cases} 0 \le P_{\mathrm{csp,sto,in},k,t} \le \overline{P}_{\mathrm{csp,sto,in},k}, \\ 0 \le P_{\mathrm{csp,sto,out},k,t} \le \overline{P}_{\mathrm{csp,sto,out},k}, \\ P_{\mathrm{csp,sto,in},k,t} P_{\mathrm{csp,sto,out},k,t} = 0, \end{cases} \tag{25}$$

where $\overline{P}_{\mathrm{csp,sto,in},k}$ and $\overline{P}_{\mathrm{csp,sto,out},k}$ denote the maximum charging and discharging powers, respectively. The thermal-storage state evolves according to

$$S_{\mathrm{csp},k,t+1} = S_{\mathrm{csp},k,t} + \eta_{\mathrm{ch}} P_{\mathrm{csp,sto,in},k,t} \Delta t - \frac{P_{\mathrm{csp,sto,out},k,t} \Delta t}{\eta_{\mathrm{dis}}}, \tag{26}$$

subject to

$$S_{\mathrm{csp},k}^{\min} \le S_{\mathrm{csp},k,t} \le S_{\mathrm{csp},k}^{\max}, \qquad t \in \mathcal{T}. \tag{27}$$

here, $S_{\mathrm{csp},k,t}$ denotes the thermal-energy-storage state, $S_{\mathrm{csp},k}^{\min}$ and $S_{\mathrm{csp},k}^{\max}$ denote its lower and upper bounds, and η_{ch} and η_{dis} denote the charging and discharging efficiencies. The CSP agent therefore combines renewable generation availability with storage-supported ramping flexibility in the allocation process.

4.3 Perception and Node-Aware Feature Representation

At iteration n, each agent evaluates candidate nodes relative to the current shared environment $\mathcal{E}^{(n)}$. For a candidate node m, the evaluation is performed through a virtual reassignment of agent k to m while the states of the remaining agents are retained. The candidate state is used only for local evaluation until the corresponding action is accepted.

The node-aware feature label characterizes the normalized intra-day generation profile of agent k at candidate node m. The label provides a compact representation of temporal resource characteristics for local resource–load matching, while the complete chronological hourly profiles are retained for accommodation and network-feasibility evaluation. The 24-dimensional feature label is defined as

$$\boldsymbol{\Psi}_{k,m}^{(n)} = \left[\phi_{k,m,1}^{(n)}, \phi_{k,m,2}^{(n)}, \ldots, \phi_{k,m,24}^{(n)} \right]. \tag{28}$$

The h-th element is calculated as

$$\phi_{k,m,h}^{(n)} = \frac{\sum_{d=0}^{364} P_{k,m,d\times 24+h}^{\mathrm{prof},(n)}}{\max_{h' \in \{1,\ldots,24\}} \left(\sum_{d=0}^{364} P_{k,m,d\times 24+h'}^{\mathrm{prof},(n)} \right) + \varepsilon}, \tag{29}$$

where h is the hour index, d is the day index, $P_{k,m,t}^{\mathrm{prof},(n)}$ denotes the chronological candidate generation profile of agent k at node m, and ε is a small positive constant used to avoid division by zero. For wind, PV, and

CSP agents, $P_{k,m,t}^{\mathrm{prof},(n)}$ is constructed from the corresponding available-generation profile. For hydropower and thermal-power agents, it is constructed from the feasible dispatchable-output profile.

The load-matching distance between agent k and candidate node m is

$$\lambda_{k,m}^{\mathrm{load},(n)} = \frac{1}{24}\sum_{h=1}^{24}\left|\phi_{k,m,h}^{(n)} - \phi_{m,h}^{\mathrm{load}}\right|, \tag{30}$$

where $\phi_{m,h}^{\mathrm{load}}$ is the normalized load label of node m at hour h. A smaller value indicates closer temporal compatibility between the candidate generation profile and the nodal load profile.

The candidate annual accommodated energy used in local evaluation is

$$E_{k,m}^{\mathrm{acc},(n)} = \sum_{t\in\mathcal{T}} P_{k,m,t}^{\mathrm{acc},(n)}\Delta t, \tag{31}$$

where $P_{k,m,t}^{\mathrm{acc},(n)}$ is the accommodated active-power output associated with the candidate allocation.

The grid-related perception of a candidate node is represented by three non-negative violation measures, $V_{k,m}^{\mathrm{cap},(n)}$, $V_{k,m}^{\mathrm{ramp},(n)}$, and $V_{k,m}^{\mathrm{sec},(n)}$, corresponding to nodal capacity allocation, ramping capability, and transmission-section loading, respectively. Each measure is zero when the corresponding constraint class is satisfied and positive when the candidate allocation produces a violation. The candidate-node perception available to agent k is summarized as

$$\mathbf{p}_{k,m}^{(n)} = \left[E_{k,m}^{\mathrm{acc},(n)}, \lambda_{k,m}^{\mathrm{load},(n)}, V_{k,m}^{\mathrm{cap},(n)}, V_{k,m}^{\mathrm{ramp},(n)}, V_{k,m}^{\mathrm{sec},(n)}\right]. \tag{32}$$

The 24-dimensional label primarily captures intra-day complementarity because the same hourly position is aggregated across the annual horizon. Seasonal variation is retained in the chronological hourly profiles used for accommodation and network evaluation.

4.4 Agent-Level Fitness Function

The candidate-node perception is converted into a local decision score through an agent-level fitness function. For agent k and candidate node m at iteration n, the fitness is defined as

$$F_{k,m}^{(n)} = \overline{E}_{k,m}^{\mathrm{acc},(n)} - \eta\overline{\lambda}_{k,m}^{\mathrm{load},(n)} - \xi\overline{\Omega}_{k,m}^{(n)}, \tag{33}$$

where $\overline{E}_{k,m}^{\mathrm{acc},(n)}$, $\overline{\lambda}_{k,m}^{\mathrm{load},(n)}$, and $\overline{\Omega}_{k,m}^{(n)}$ denote normalized candidate accommodation, load-matching distance, and grid-constraint penalty, respectively. The coefficients η and ξ control the relative contributions of temporal resource–load matching and grid-related feedback to local candidate evaluation.

For a non-negative candidate indicator $X_{k,m}^{(n)}$, normalization over the candidate-node set is performed as

$$\overline{X}_{k,m}^{(n)} = \frac{X_{k,m}^{(n)}}{\max_{m'\in\mathcal{N}} X_{k,m'}^{(n)} + \varepsilon}. \tag{34}$$

The grid-constraint penalty is calculated from the capacity, ramping, and transmission-section violation measures:

$$\Omega_{k,m}^{(n)} = \omega_{\mathrm{cap}} V_{k,m}^{\mathrm{cap},(n)} + \omega_{\mathrm{ramp}} V_{k,m}^{\mathrm{ramp},(n)} + \omega_{\mathrm{sec}} V_{k,m}^{\mathrm{sec},(n)}, \tag{35}$$

where ω_{cap}, ω_{ramp}, and ω_{sec} are fixed penalty weights. The penalty incorporates constraint-violation severity into local ranking, allowing candidate nodes with similar accommodation and load-matching characteristics to be differentiated according to their effects on the constrained grid environment.

Constraint penalties rank local candidates according to violation severity, and hard feasibility screening determines whether a candidate state transition is admissible. This two-stage structure separates candidate ranking from transition acceptance.

4.5 Migration and Cooperation Actions

Agent actions are defined over the current state and candidate-node perceptions. For an individual agent, the local action consists of retaining the current node or testing migration to a candidate node. Pairwise cooperation provides an additional local interaction in which two capacity-block agents are evaluated jointly at a common candidate node. The action space is represented as

$$\mathcal{A}_k^{(n)} = \{\text{stay}\} \cup \{\text{migrate}(m) : m \in \mathcal{N}\} \cup \{\text{cooperate}(l, m) : l \in \mathcal{K}\backslash\{k\},\ m \in \mathcal{N}\}. \tag{36}$$

For migration, a candidate node m is feasible only when the capacity, ramping, and transmission-section conditions are simultaneously satisfied. The corresponding feasibility indicator is

$$\chi_{k,m}^{(n)} = \begin{cases} 1, & V_{k,m}^{\text{cap},(n)} = V_{k,m}^{\text{ramp},(n)} = V_{k,m}^{\text{sec},(n)} = 0, \\ 0, & \text{otherwise.} \end{cases} \tag{37}$$

A tested migration from the current node $m_k^{(n)}$ to candidate node m is accepted when the candidate improves the local fitness and passes the feasibility screen. The resulting node-state transition is

$$m_k^{(n+1)} = \begin{cases} m, & F_{k,m}^{(n)} > F_{k,m_k^{(n)}}^{(n)} \text{ and } \chi_{k,m}^{(n)} = 1, \\ m_k^{(n)}, & \text{otherwise.} \end{cases} \tag{38}$$

Cooperation is implemented as a temporary pairwise joint evaluation. For agents k and l evaluated at a common node m, a joint feature label is calculated from the aggregated output profile of the pair. Let $\lambda_{k,l,m}^{\text{load},(n)}$ denote the corresponding load-matching distance. The pair satisfies the matching condition when

$$\begin{cases} \lambda_{k,m}^{\text{load},(n)} \geq \lambda_{k,l,m}^{\text{load},(n)}, \\ \lambda_{l,m}^{\text{load},(n)} \geq \lambda_{k,l,m}^{\text{load},(n)}. \end{cases} \tag{39}$$

The joint candidate is retained only when its local fitness is no worse than the individual alternatives:

$$F_{k\cup l,m}^{(n)} \geq \max\left\{F_{k,m}^{(n)}, F_{l,m}^{(n)}\right\}, \tag{40}$$

where $F_{k\cup l,m}^{(n)}$ denotes the fitness calculated from the temporarily aggregated output profile of the pair. The notation $k \cup l$ represents joint evaluation only; agents k and l retain their individual identities, capacities, and membership in $\mathcal{K}$. Any cooperative candidate is subjected to the same grid-feasibility screening before the cooperative configuration is retained.

4.6 State Transition, Grid Feedback, and Iterative Procedure

An accepted local action changes the corresponding agent-node assignment and consequently modifies the shared grid environment. After each accepted migration or cooperative configuration, the nodal capacity allocation, active-power injections, residual demands, and transmission flows are recalculated according to the system model in Section 3. The updated capacity, ramping, and transmission-section conditions are then used in subsequent candidate-node evaluations. Rejected candidates leave the current agent state and grid environment unchanged.

Agent evaluations are scheduled sequentially. Once an accepted local action changes the current allocation, the shared environment is refreshed before the next local decision is evaluated. The resulting computational loop therefore consists of agent-state evaluation, candidate-node perception, local fitness evaluation, migration or cooperation, feasibility screening, state updating, and grid-feedback renewal. The centralized program coordinates this simulation sequence, and allocation changes are produced by the agent-level transition rules defined above.

Fig. 1 summarizes the agent–grid feedback mechanism underlying the iterative capacity-allocation process.

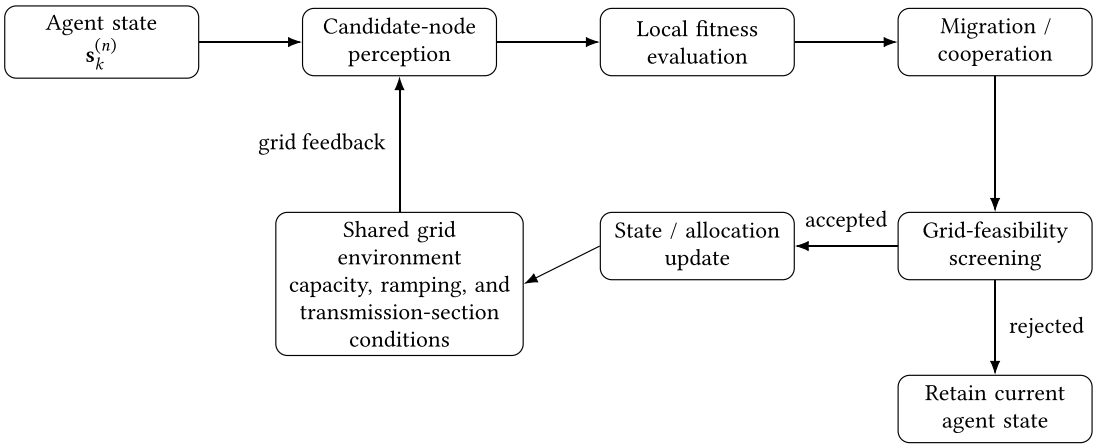


Figure 1: Agent–grid feedback mechanism of the proposed ABM.

The complete simulation procedure is summarized in Algorithm 1. The output-profile models provide the resource-specific temporal characteristics, whereas the feature representation, local fitness, migration and cooperation rules, and grid-feasibility screening determine the iterative capacity-allocation process.

Algorithm 1: Sequential agent–grid feedback procedure

Require: Agent set $\mathcal{K}$, candidate-node set $\mathcal{N}$, resource and load profiles, grid parameters, fitness and penalty weights, maximum iteration number $I_{\max}$
Ensure: Final capacity allocation and evaluation performance indicators
1: Initialize agent-node assignments and the corresponding grid environment
2: Calculate the resource-specific output profiles
3: **for** $n = 1$ to $I_{\max}$ **do**
4: **for** each agent $k \in \mathcal{K}$ according to the simulation schedule **do**
5: **for** each tested candidate node $m \in \mathcal{N}$ **do**
6: Construct the virtual reassignment of agent k to node m

(Continued)

Algorithm 1 (continued)

Calculate the node-aware feature representation and load-matching distance
Evaluate candidate renewable accommodation and grid-constraint feedback
Calculate the local fitness $F_{k,m}^{(n)}$
end for
Test candidate migration according to the local fitness and feasibility conditions
if the tested migration is accepted **then**
Update the corresponding agent-node assignment
Recalculate the shared grid environment
else
Retain the current agent state
end if
Test eligible pairwise cooperation according to the matching and joint-fitness conditions
if the cooperative configuration is accepted and feasible **then**
Retain the cooperative configuration
Recalculate the shared grid environment
end if
end for
Record system-level and agent-level performance indicators
end for
return final capacity allocation and evaluation performance indicators

The reported experiments use a fixed 500-iteration horizon. Convergence is assessed from the evolution trajectories reported in Section 5, with particular attention to the stabilization of system-level annual non-hydro renewable accommodation.

Let $K_a = |\mathcal{K}|$ and $M = |\mathcal{N}|$. Over I iterations, testing candidate nodes requires up to $O(IK_aM)$ agent–node evaluations. If all agent pairs are examined for cooperation, the pairwise interaction stage introduces up to $O(IK_a^2)$ pair tests. The two complexity bounds count candidate-node and pairwise evaluations. Total runtime additionally includes the annual-profile calculations and grid-feasibility assessments performed for each tested candidate.

5 Case Study and Experimental Results

5.1 Case Description and Evaluation Protocol

The case study is based on an anonymized provincial transmission network in China. The network contains 34 anonymized nodes interconnected by 330 and 750 kV transmission lines and is organized into seven operating regions with seven monitored transmission sections. The generation portfolio includes wind power, PV, hydropower, thermal power, and CSP. The total capacity of each generation type remains fixed during allocation, while the nodal assignments of the corresponding discrete capacity blocks can change. Fig. 2 presents the anonymized network topology and initial generation-resource distribution.

The annual evaluation horizon contains 8760 hourly intervals with $\Delta t = 1$ h. Chronological wind-resource, solar-resource, and nodal-load profiles retain their temporal ordering throughout the annual evaluation. Geographical identifiers and raw hourly operational profiles are anonymized under grid-data confidentiality restrictions. The principal system and resource configurations are summarized in Table 1.

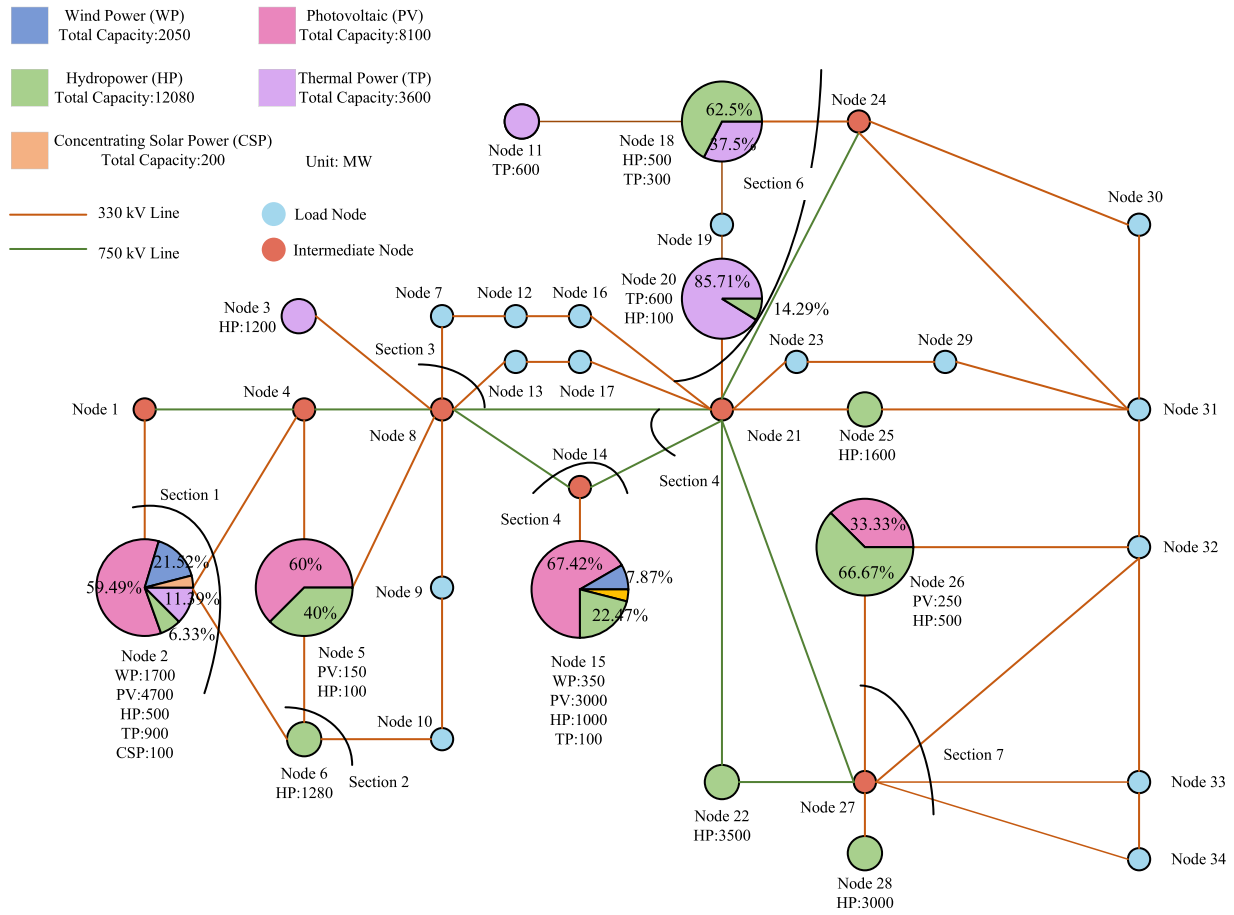


Figure 2: Anonymized provincial transmission-network structure and generation-resource distribution. The percentage labels indicate the generation-resource composition of the corresponding nodes or regional generation clusters shown by the pie charts. WP, PV, HP, TP, and CSP denote wind power, photovoltaic power, hydropower, thermal power, and concentrating solar power, respectively.

Table 1: Case-system and resource configuration.

Item	Case Specification
Network type	Anonymized provincial transmission network in China
Voltage levels	330 kV and 750 kV
Network nodes	34 anonymized nodes
Operating regions	7
Monitored transmission sections	7
Evaluation horizon	One year, $\lvert\mathcal{T}\rvert = 8760$, $\Delta t = 1$ h
Generation portfolio	Wind: 2050 MW; PV: 8100 MW; hydropower: 12080 MW; thermal power: 3600 MW; CSP: 200 MW; total: 26030 MW
Renewable-resource inputs	Node-specific chronological hourly wind and solar resource profiles
Load inputs	Node-specific chronological hourly active-power demand profiles

(Continued)

Table 1 (continued)

Item	Case Specification
Capacity representation	Discrete generation-capacity blocks with fixed generation type and block capacity; nodal assignment is the planning variable
Nodal allocation bound	$\bar{C}_{g,m}$, the fixed admissible planning-allocation limit of generation type g at node m
Transmission-section bound	$F_q^{\max}$, the fixed admissible active-power transfer limit of monitored transmission section q

The nodal bound $\bar{C}_{g,m}$ represents the case-specific admissible planning-allocation limit for generation type g at node m under the adopted DCPF-based planning model. The transmission-section limit $F_q^{\max}$ specifies the corresponding admissible active-power transfer limit for monitored section q. Both quantities are fixed case inputs and are applied consistently across all compared schemes together with the same generation-output and ramping constraints. The algorithmic and numerical settings are summarized in Table 2.

Table 2: Simulation settings.

Item	Setting
Proposed ABM iteration budget	500 iterations; fixed evaluation horizon
Linear-migration iterations	100
PSO-DC swarm size	15 particles
PSO-DC inertia weight	$\omega_{\text{pso}} = 0.80$
PSO-DC acceleration coefficients	$c_1 = 0.50$, $c_2 = 0.20$
PSO-DC iteration budget	500 iterations; fixed maximum
MILP-DC execution	One centralized optimization solve for each deterministic case evaluation
Feature-label dimension	24
Power-flow representation	DCPF
System-level objective	Maximization of annual non-hydro renewable accommodation
Reported performance indicators	Annual non-hydro renewable accommodation, annual non-hydro renewable curtailment, non-hydro renewable curtailment rate, agent-level annual accommodation, and short-term aggregated wind–PV–CSP output variation
ABM fitness weights	$\eta = 0.30$, $\xi = 0.70$
ABM penalty weights	$\omega_{\text{cap}} = 1.00$, $\omega_{\text{ramp}} = 1.50$, $\omega_{\text{sec}} = 2.00$
Normalization constant	$\varepsilon = 10^{-8}$
Stochastic evaluation	10 independent random seeds for the proposed ABM and PSO-DC
MILP-DC solver tolerance	Relative optimality gap = 10^{-4}
Software environment	MATLAB R2023b; Python 3.10.13; NumPy 1.26.4; Pandas 2.2.2; Matplotlib 3.8.4; Gurobi 10.0.3

Note: ABM denotes agent-based model; DCPF denotes direct-current power flow; PSO-DC denotes particle swarm optimization under the DCPF formulation; MILP-DC denotes mixed-integer linear programming under the DCPF formulation.

Five allocation schemes are evaluated under the same chronological case data and planning constraints. The original allocation represents the initial reference configuration, and the linear migration scheme provides a simple resource-oriented baseline. Mixed-integer linear programming under the DCPF formulation (MILP-DC) provides a centralized optimization benchmark for the formulated static capacity-allocation problem, whereas particle swarm optimization under the DCPF formulation (PSO-DC) provides

a population-based heuristic benchmark. Recent power-system studies have applied particle swarm optimization (PSO) to transmission-network planning and renewable-energy dispatch [46,47]. The proposed ABM generates capacity allocations through sequential candidate-node evaluation, local migration and cooperation, feasibility screening, and grid-feedback updating.

In PSO-DC, each particle represents a complete candidate allocation of the prescribed generation-capacity blocks. The initial swarm is randomly generated over the candidate allocation space. Each particle position is decoded into the binary assignment matrix $\mathbf{z}$, in which every capacity block is assigned to one candidate node while the prescribed total capacity of each generation type is preserved. The decoded allocation is evaluated using the system-level annual non-hydro renewable accommodation objective E^{acc} together with the adopted DCPF-based planning constraints.

For particle i at iteration r, the velocity and position are updated according to the inertia-weight PSO mechanism [47]:

$$\begin{aligned}\mathbf{v}_i^{r+1} &= \omega_{\mathrm{pso}}\mathbf{v}_i^r + c_1 r_{1,i}^r\left(\mathbf{p}_i^r - \mathbf{x}_i^r\right) + c_2 r_{2,i}^r\left(\mathbf{g}^r - \mathbf{x}_i^r\right),\\ \mathbf{x}_i^{r+1} &= \mathbf{x}_i^r + \mathbf{v}_i^{r+1},\end{aligned} \tag{41}$$

where $\mathbf{x}_i^r$ and $\mathbf{v}_i^r$ denote the position and velocity of particle i, $\mathbf{p}_i^r$ denotes its personal-best position, $\mathbf{g}^r$ denotes the global-best position, and $r_{1,i}^r$ and $r_{2,i}^r$ are independent random variables uniformly distributed over $[0,1]$. The parameters ω_{pso}, c_1, and c_2 denote the inertia, cognitive, and social coefficients, respectively.

After each position update, the particle is decoded into a candidate capacity allocation and evaluated using the common DCPF-based planning-feasibility conditions. Feasible candidate allocations participate in personal-best and global-best updates according to the system-level annual non-hydro renewable accommodation E^{acc}. The ABM local fitness and the PSO-DC particle evaluation therefore operate at different decision levels: the former guides agent-level candidate selection, while the latter evaluates complete system-level allocations. After the prescribed iteration budget, the feasible global-best particle determines the final PSO-DC capacity allocation.

The PSO-DC hyperparameters are fixed across all independent runs. A moderate swarm size limits the number of annual-profile and DCPF evaluations performed in each iteration, while the iteration budget is aligned with that of the proposed ABM to provide a consistent search horizon. The complete PSO-DC parameter settings are reported in Table 2.

All compared schemes use the same chronological case data and planning-feasibility setting, so the comparison isolates differences among capacity-allocation mechanisms.

5.2 Overall Performance against Reference and Optimization Benchmarks

Table 3 evaluates the proposed ABM from three complementary perspectives: improvement over the original allocation, comparison with the generic PSO-DC heuristic search, and proximity to the centralized MILP-DC benchmark.

Relative to the original allocation, the proposed ABM increases annual non-hydro renewable accommodation from 15,778,553.09 to 16,008,253.75 MWh, corresponding to an increase of approximately 1.46%. The gain is concentrated in PV and CSP accommodation, while wind accommodation decreases slightly. The resulting system-level improvement reflects a redistribution of accommodation among heterogeneous renewable resources under the revised nodal allocation.

Table 3: Aggregate performance against the reference case and optimization benchmarks.

Indicator	Unit	Original	PSO-DC	Proposed ABM	MILP-DC
Wind accommodation	MWh	3,814,633.32	3,790,500.00 ± 9480	3,777,453.94 ± 6800	3,825,410.25
PV accommodation	MWh	11,694,279.13	11,830,000.00 ± 41,400	11,945,726.52 ± 29,900	12,094,360.50
CSP accommodation	MWh	269,640.64	274,900.00 ± 2200	285,073.28 ± 1710	299,329.25
Hydropower generation	MWh	52,509,690.23	52,418,198.20 ± 26,200	52,326,706.18 ± 20,900	52,150,000.00
Thermal power generation	MWh	10,758,104.98	10,754,900.23 ± 12,900	10,751,700.00 ± 10,800	10,717,559.93
Non-hydro renewable accommodation	MWh	15,778,553.09	15,895,400.00 ± 47,700	16,008,253.75 ± 35,200	16,219,100.00
Non-hydro renewable curtailment	MWh	2,426,876.76	2,530,850.46 ± 13,900	2,686,827.65 ± 10,700	2,561,400.00
Non-hydro renewable curtailment rate	%	13.33	13.74 ± 0.07	14.37 ± 0.06	13.64

Note: Original denotes the reference allocation. PSO-DC and MILP-DC denote the heuristic and centralized DCPF-based optimization benchmarks, respectively. Results for PSO-DC and Proposed ABM are reported as mean ± standard deviation over 10 independent runs.

Compared with PSO-DC, the proposed ABM increases annual non-hydro renewable accommodation from 15,895,400.00 to 16,008,253.75 MWh, corresponding to an increase of approximately 0.71%. In the tested case, the combination of node-aware candidate evaluation, local migration and cooperation, feasibility screening, and sequential grid feedback leads to a higher final accommodation level than the generic population-based search.

MILP-DC achieves 16,219,100.00 MWh of annual non-hydro renewable accommodation under the same static DCPF-based planning formulation. The proposed ABM reaches approximately 98.7% of this centralized benchmark, corresponding to an accommodation gap of approximately 1.30%. The 1.30% gap quantifies the difference between the locally evolving allocation process and the centralized system-level solution under the adopted formulation.

The increase in accommodation is accompanied by higher curtailment. Relative to the original allocation, annual non-hydro renewable curtailment increases from 2,426,876.76 to 2,686,827.65 MWh, while the curtailment rate increases from 13.33% to 14.37%. The proposed ABM also exhibits a higher curtailment rate than PSO-DC and MILP-DC in the reported case. Annual non-hydro renewable accommodation is the system-level optimization objective, while curtailment and curtailment rate are reported as complementary indicators of the resulting network operating condition. The simultaneous increase in accommodation and curtailment reveals an accommodation–congestion trade-off under the adopted transmission constraints.

5.3 Agent-Level Adaptation and Grid-Feedback Evolution

Fig. 3 shows the agent-level annual accommodation trajectories of the three non-hydro renewable types during allocation evolution. PV accommodation increases gradually, whereas wind accommodation reaches a relatively stable level earlier. The contrasting trajectories are consistent with the resource-specific temporal profiles and node-aware candidate evaluation, in which annual accommodation and load-shape compatibility jointly influence candidate-node fitness. The wind trajectory indicates limited additional improvement after a locally favorable allocation is reached, whereas PV continues to adjust toward nodes with stronger temporal compatibility.

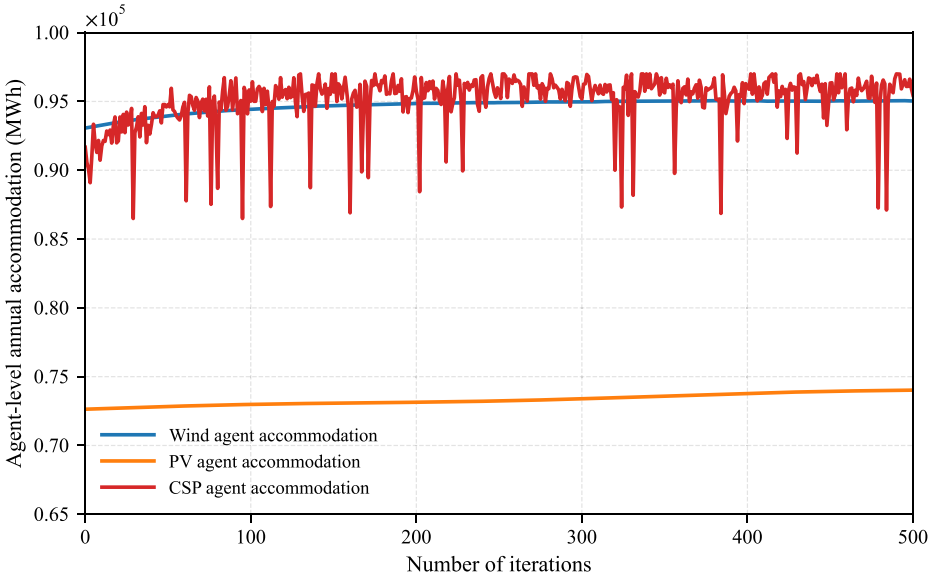


Figure 3: Agent-level accommodation evolution by non-hydro renewable type.

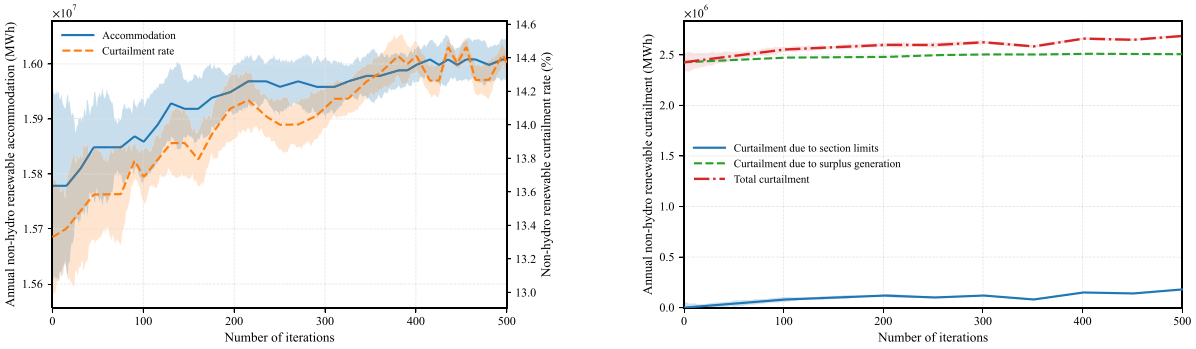
CSP exhibits larger fluctuations than wind and PV. The larger variation is consistent with its solar-driven generation profile and storage-supported intertemporal flexibility, which make candidate evaluation more responsive to changes in local resource–load and grid-feasibility conditions. Overall, the distinct trajectories indicate heterogeneous responses to the common allocation mechanism and support resource-specific temporal matching in candidate-node evaluation.

Fig. 4 shows the system-level evolution of non-hydro renewable accommodation and curtailment during ABM iterations. Annual accommodation increases gradually and then stabilizes, while the curtailment rate rises in the later stage. As capacity reassignments alter the nodal distribution of generation, the corresponding injections and transmission-section loading conditions are continuously updated. The curtailment decomposition shows an increasing contribution from section-limit curtailment, indicating stronger interaction between the evolving allocation and transmission constraints. The joint evolution reveals an accommodation–congestion trade-off in which higher renewable accommodation is accompanied by increased congestion-related curtailment. The observed trade-off supports joint evaluation of renewable accommodation and transmission-section loading in capacity-allocation decisions.

5.4 Comparison with the Linear-Migration Baseline

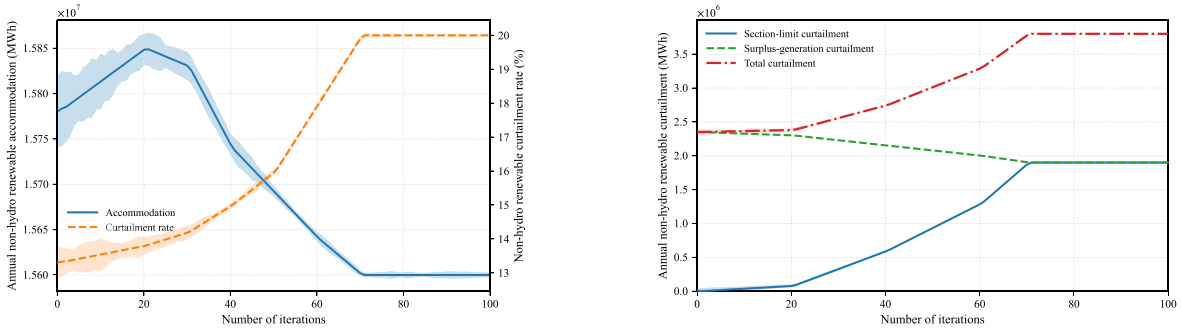
The linear-migration scheme provides a mechanism-oriented baseline based on accommodated-energy ranking. Within each non-hydro renewable generation type, capacity is successively reassigned toward nodes with higher accommodated-energy levels. The proposed ABM further incorporates temporal resource–load matching and grid-related feedback from capacity, ramping, and transmission-section constraints during candidate-node evaluation.

Fig. 5 shows that the baseline initially increases annual non-hydro renewable accommodation, followed by a turning point and subsequent decline as the iterations proceed. Meanwhile, the curtailment rate continues to rise. The curtailment decomposition further shows a pronounced increase in section-limit curtailment, while surplus-generation curtailment gradually decreases. The baseline trajectory is consistent with successive reallocations concentrating nodal injections at locally attractive nodes and increasing interaction with constrained transmission sections.



(A) ABM accommodation–curtailment trajectory (B) ABM curtailment decomposition

Figure 4: System-level accommodation and curtailment evolution.



(A) Baseline accommodation–curtailment trajectory (B) Baseline curtailment decomposition

Figure 5: Linear-migration baseline evolution.

The baseline therefore provides a mechanism-oriented contrast for evaluating the role of temporal matching and grid-feedback information in successive capacity reassignment. Local accommodation ranking can support initial allocation gains, whereas sustained improvement also depends on distinguishing candidate nodes according to their temporal compatibility and transmission consequences.

5.5 Final Capacity Allocation

Table 4 presents the final nodal capacity allocation generated by the proposed ABM. The prescribed capacity portfolio of each generation type is maintained, while individual capacity blocks are redistributed across candidate nodes through successive migration and cooperation. The resulting allocation exhibits a heterogeneous spatial pattern across wind, PV, hydropower, thermal power, and CSP, reflecting the differentiated responses of generation resources to local accommodation conditions, temporal resource–load compatibility, and grid-related evaluation.

The final configuration translates the iterative agent-level adaptation process into a system-level spatial allocation of generation capacity. Differences in nodal resource characteristics and local evaluation outcomes lead to distinct allocation patterns among generation types, providing the spatial basis for the accommodation and congestion behavior observed at the system level.

Table 4: Final capacity allocation.

Node	Wind	PV	Hydro	Thermal	CSP
2	1300	6000	10 × 50	3 × 300	200
3	–	–	–	2 × 600	–
5	–	1050	2 × 50	–	–
6	–	–	4 × 320	–	–
11	–	–	–	2 × 300	–
15	750	1050	10 × 100	–	–
18	–	–	5 × 100	2 × 150	–
20	–	–	2 × 50	2 × 300	–
22	–	–	5 × 700	–	–
25	–	–	4 × 400	–	–
26	–	–	10 × 50	–	–
28	–	–	10 × 300	–	–

Note: All capacity values are in MW. Entries of the form $n \times c$ denote n discrete capacity blocks of c MW each. "–" denotes no allocated capacity. CSP denotes concentrating solar power.

5.6 Short-Term Wind–PV–CSP Output Analysis

Fig. 6 compares the five-day aggregated output profiles of wind, PV, and CSP generation under the original and proposed ABM allocations. Both profiles retain the characteristic diurnal variation of the combined renewable resources, while differences in peak magnitude and off-peak output emerge across the selected period. The profile differences reflect the effect of nodal capacity reallocation on short-term renewable output patterns and provide a temporal complement to the annual accommodation and curtailment results.

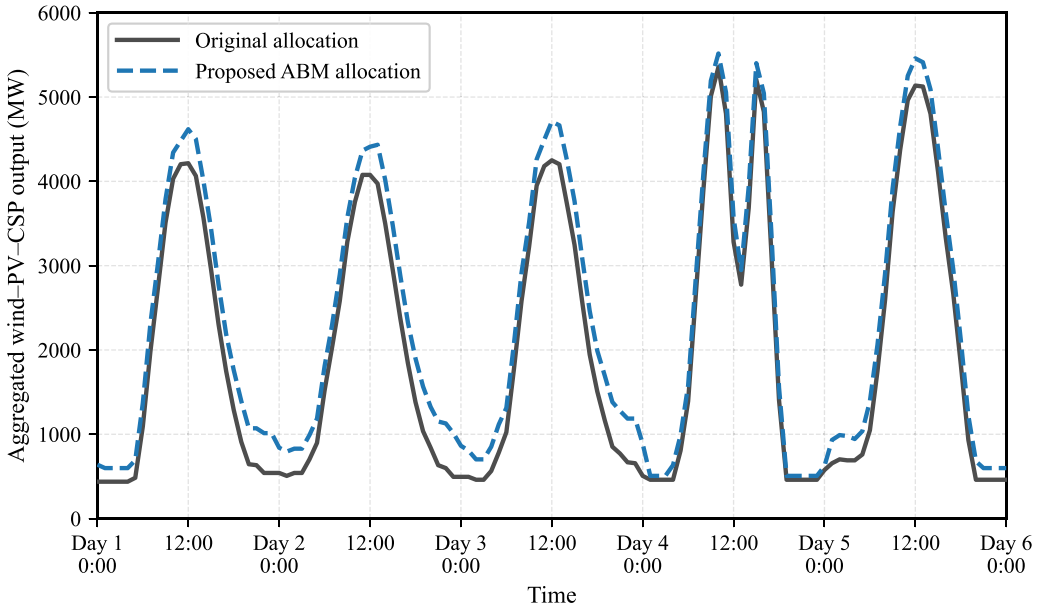


Figure 6: Five-day aggregated wind–PV–CSP output profiles.

5.7 Sensitivity and Ablation Analysis

Table 5 evaluates the influence of temporal feature resolution on non-hydro renewable accommodation. Increasing the representation from 3D and 6D to the 24D hourly descriptor progressively improves accommodation, showing that finer intra-day information provides greater discrimination among candidate nodes with different temporal resource–load characteristics. The higher temporal resolution is accompanied by additional computational cost, reflecting a trade-off between representation granularity and evaluation efficiency. The 24D feature representation is adopted in the main experiments.

Table 5: feature representation comparison.

Feature Representation	Dimension	Non-Hydro Renewable Accommodation (MWh)	Computational Time (s)
Peak/valley/normal baseline	3D	15,850,000	**450**
Time-of-use representation	6D	15,920,000	620
Proposed feature-label representation	24D	**16,008,253**	980

Note: Bold values indicate the highest accommodation and the shortest computational time, respectively.

Table 6 compares alternative metrics for temporal resource–load matching. The normalized L_1 distance achieves the highest non-hydro renewable accommodation together with the lowest curtailment rate and computational time among the tested metrics. The element-wise absolute-difference formulation directly measures normalized hourly profile mismatch and provides a consistent basis for candidate-node comparison. The normalized L_1 distance is therefore used in the subsequent experiments.

Table 6: Load-shape matching metric comparison.

Matching Metric	Non-Hydro Renewable Accommodation (MWh)	Non-Hydro Renewable Curtailment Rate (%)	Computational Time (s)
Proposed normalized L_1 distance	**16,008,253**	**14.37**	**980**
Euclidean distance	15,974,680	14.46	985
Cosine distance	15,936,420	14.58	992
Pearson-correlation distance	15,921,870	14.63	1006

Note: Bold values indicate the highest accommodation, the lowest curtailment rate, and the shortest computational time among the tested metrics.

Table 7 examines the sensitivity of the agent-level fitness to the weights η and ξ. Annual non-hydro renewable accommodation remains within a relatively narrow range across the tested settings, whereas the curtailment rate exhibits a clearer response to changes in the constraint-related weight. The baseline setting $(\eta, \xi) = (0.30, 0.70)$ yields the highest accommodation, while increasing ξ to 0.90 reduces the curtailment rate with a corresponding decrease in accommodation. The observed response shows that the fitness weights regulate the balance among temporal matching, renewable accommodation, and grid-related constraints during candidate-node evaluation.

Table 8 evaluates the contribution of the principal components of the proposed framework. Removing the feature-label mechanism produces the largest reduction in non-hydro renewable accommodation, highlighting the importance of temporal representation in candidate-node evaluation. Removing either the migration rule or the temporal–spatial index also decreases accommodation, showing that adaptive capacity

reassignment and temporal–spatial information both contribute to the allocation process. The combined removal produces a larger reduction than either individual removal, indicating complementary roles for the migration rule and temporal–spatial information in shaping the final system-level allocation.

Table 7: Fitness-weight sensitivity analysis.

η	ξ	Non-Hydro Renewable Accommodation (MWh)	Non-Hydro Renewable Curtailment Rate (%)	Remark
0.20	0.70	15,958,620	14.52	Low load-matching weight
0.30	0.50	15,973,480	14.86	Weak constraint penalty
0.30	0.70	16,008,253	14.37	Baseline setting
0.30	0.90	15,941,760	13.98	Strong constraint penalty
0.40	0.70	15,989,340	14.41	Strong load-matching weight

Note: The baseline setting $(\eta, \xi) = (0.30, 0.70)$ is used in the main experiments.

Table 8: Model ablation study.

Model Configuration	Feature-Label Mechanism	Migration Rule	Temporal–Spatial Index	Non-Hydro Renewable Accommodation (MWh)	Relative Accommodation Change
Full model	✓	✓	✓	16,008,253	–
Variant I w/o feature label	×	✓	✓	15,790,120	−1.36%
Variant II w/o migration	✓	×	✓	15,885,400	−0.77%
Variant III w/o temporal–spatial index	✓	✓	×	15,910,350	−0.61%
Variant IV w/o migration and index	✓	×	×	15,815,600	−1.20%

Note: "✓" indicates that the component is retained, and "×" indicates that the component is removed. Relative accommodation change is calculated with respect to the full model.

6 Discussion and Limitations

6.1 Mechanistic Interpretation of Local Adaptation

The allocation process is driven by the interaction among temporal representation, local candidate evaluation, and grid feedback. The node-aware feature label preserves the intra-day characteristics of generation output, while the load-shape matching term distinguishes candidate nodes according to temporal compatibility with local demand. The feature and matching signals are combined with non-hydro renewable accommodation and grid-constraint information in the agent-level fitness, allowing migration and cooperation decisions to respond jointly to resource conditions, load characteristics, and network states.

Accepted capacity reassignments modify nodal injections, residual demand, and transmission flows and thereby update the shared environment for later agent evaluations. The resulting feedback loop connects individual capacity-block decisions with the evolving system state and enables the final nodal allocation to emerge through successive local adaptations. Sensitivity and ablation results further show that temporal feature representation, migration, and temporal–spatial information jointly influence accommodation performance.

6.2 Accommodation–Congestion Trade-Off

The final allocation increases annual non-hydro renewable accommodation while also producing a higher curtailment level. The concurrent increase in accommodation and curtailment reflects the interaction between improved local resource–load compatibility and finite transmission capability. Capacity reassignment toward nodes with favorable accommodation potential increases the amount of renewable generation that can be utilized over the year, while the resulting spatial redistribution of nodal injections also changes the loading of monitored transmission sections.

As renewable capacity becomes concentrated at locally attractive nodes, a larger share of available generation can encounter transmission bottlenecks during periods of high output. The increase in section-related curtailment therefore accompanies the gain in absolute accommodation, forming an accommodation–congestion trade-off under the adopted transmission-section constraints. The accommodation–congestion trade-off indicates that renewable-generation capacity allocation should be evaluated jointly through accommodation, curtailment, and transmission-congestion indicators, since higher annual renewable utilization can coexist with stronger local transmission pressure.

6.3 Modeling Boundary and Engineering Implications

The adopted DCPF formulation represents the active-power transfer effects of nodal capacity reallocation at the planning level. Capacity limits, generation-output bounds, ramping capability, power balance, and transmission-section constraints define the network conditions considered during agent evaluation and feasibility screening. The resulting allocation therefore provides a strategic active-power planning representation of the interaction among spatial capacity distribution, temporal resource–load characteristics, renewable accommodation, and transmission congestion.

Reactive-power flow, voltage magnitude, network losses, AC security, and dynamic stability belong to a more detailed operational assessment layer. Such operational characteristics become increasingly important as candidate allocations approach network operating limits and should be incorporated when progressing from planning-level screening to implementation-oriented studies. The current case study establishes the spatial allocation and congestion characteristics that can guide subsequent AC power-flow, security, and operational analyses.

From an engineering perspective, the observed congestion response indicates that generation-capacity reallocation and transmission capability should be coordinated in renewable-rich systems. Regions associated with stronger transmission constraints may benefit from targeted transmission reinforcement, storage deployment, flexible dispatchable resources, or demand-side flexibility. The framework can support this planning process by identifying capacity-allocation patterns and transmission-congestion interactions before detailed investment and operational decisions are undertaken. Validation on additional transmission networks and operating conditions would further establish the applicability of these findings across different system structures and renewable-resource compositions.

7 Conclusion

This study developed a grid-aware agent-based computational framework for generation-capacity allocation in renewable-rich power systems. Planned generation-capacity increments are represented as adaptive agents whose local migration and cooperation decisions are guided by temporal resource–load matching, renewable accommodation, and network-constraint feedback. Through repeated state updates and grid feedback, the framework establishes an explicit connection between agent-level adaptation and the resulting nodal capacity allocation.

In the anonymized provincial transmission-network case, the proposed framework increases annual non-hydro renewable accommodation from 15.7786 to 16.0083 million MWh, corresponding to an improvement of approximately 1.46%. The resulting accommodation also exceeds the PSO-DC heuristic benchmark and reaches approximately 98.7% of the centralized MILP-DC benchmark under the adopted DCPF-based planning formulation. Sensitivity and ablation results further show that temporal feature representation, adaptive migration, and temporal–spatial information contribute to allocation performance. Higher accommodation is accompanied by increased curtailment, revealing an accommodation–congestion trade-off associated with binding transmission-section constraints.

The case-study results show that renewable-generation capacity allocation is shaped jointly by local resource–load compatibility and transmission capability. The proposed framework traces the progression from local capacity adaptation to system-level accommodation and congestion outcomes. The resulting allocation patterns can support subsequent assessment of network reinforcement and flexibility measures. Future work will extend the planning formulation toward AC-security assessment, investment-aware decision making, and validation across additional transmission-network cases.

Acknowledgement: Not applicable.

Funding Statement: This work was supported in part by the Science and Technology Project of State Grid Gansu Electric Power Company under Grant No. B22730250042 and in part by the Gansu Province Basic Research Project under Grant No. 26JRZA06. State Grid Gansu Electric Power Company provided access to the transmission-network data and operational profiles used in this study under institutional confidentiality requirements. The research design, data analysis, and manuscript preparation were conducted by the authors. The funding organizations did not exercise control over the interpretation of the findings or the decision to submit the manuscript for publication.

Author Contributions: Conceptualization, Shenglei Du and Qinjuan Wang; methodology, Shenglei Du and Zhuxiu Wang; software, Shenglei Du and Zhaobin Li; validation, Shenglei Du, Qinjuan Wang and Yalu Sun; formal analysis, Shenglei Du; investigation, Qinjuan Wang and Yalu Sun; resources, Qinjuan Wang and Yalu Sun; data curation, Shenglei Du; writing—original draft preparation, Shenglei Du and Zhuxiu Wang; writing—review and editing, Qinjuan Wang, Yalu Sun and Zhaobin Li; visualization, Shenglei Du; supervision, Zhaobin Li; project administration, Qinjuan Wang and Zhaobin Li; funding acquisition, Zhaobin Li. All authors contributed to the article and approved the submitted version.

Availability of Data and Materials: The raw operational profiles cannot be made publicly available because of grid-data confidentiality and institutional data-use restrictions. The anonymized topology description, installed capacity settings, model equations, simulation protocol, and aggregate results are provided in the manuscript to support methodological reproducibility. Requests for additional information should be directed to the corresponding author and will be considered subject to data-confidentiality constraints.

Ethics Approval: Not applicable.

Conflicts of Interest: Qinjuan Wang, Zhuxiu Wang, and Yalu Sun are affiliated with State Grid Gansu Electric Power Company, which provided partial financial support for this research. The authors declare no other competing interests.

Abbreviations

ABM	Agent-based model
AC	Alternating current
CSP	Concentrating solar power
DCPF	Direct-current power flow
HP	Hydropower

MILP-DC	Mixed-integer linear programming under the DCPF formulation
NHR	Non-hydro renewable
PSO	Particle swarm optimization
PSO-DC	Particle swarm optimization under the DCPF formulation
PV	Photovoltaic
TP	Thermal power
WP	Wind power

References

1. Fang Y, Han J, Du E, Jiang H, Fang Y, Zhang N, et al. Electric energy system planning considering chronological renewable generation variability and uncertainty. Appl Energy. 2024;373:123961. doi:10.2139/ssrn.4795231.
2. Hu Y, Jiang H, Zhang C, Yuan J, Zhang M, Yao L, et al. Advancing solar and wind penetration in China through energy complementarity. Nature. 2026;653(8116):1060–8. doi:10.1038/s41586-026-10570-z.
3. Cai Q, Qing J, Zhong C, Xu Q, Liang QM. Temporal and spatial heterogeneity analysis of wind and solar power complementarity and source-load matching characteristics in China. Energy Convers Manag. 2024;315:118770. doi:10.1016/j.enconman.2024.118770.
4. Hu Q, Li G, Huang B, Yang Q, Sun S, Bie Z, et al. Hybrid tri-level optimal sizing of hydrogen storage for addressing long-term seasonal fluctuation of RES. IEEE Trans Sustain Energy. 2026;17(2):883–96. doi:10.1109/tste.2025.3600298.
5. Diao H, Li P, Tu C, Che L. Optimal co-planning of multi-port soft open points and energy storage systems for improving hosting capacity and operation efficiency in distribution networks. IEEE Trans Power Deliv. 2025;40(1):459–71. doi:10.1109/tpwrd.2024.3503662.
6. Wan C, Hu X, Li B, Li Y, Liu H, Ju P. A point-hyperplane geometry method for operational security region of renewable energy generation in power systems. IEEE Trans Power Syst. 2026;41(2):1308–20. doi:10.1109/tpwrs.2025.3600614.
7. Lu P, Lan H, Liu S, Zhang N, Li K, Shahidehpour M. Two-stage distributionally robust optimization dispatch for power systems with uncertain small-sample wind and photovoltaic data. IEEE Trans Smart Grid. 2026;17(1):429–41. doi:10.1109/tsg.2025.3621481.
8. Zhang Y, Jia M, Wen H, Bian Y, Shi Y. Toward value-oriented renewable energy forecasting: an iterative learning approach. IEEE Trans Smart Grid. 2025;16(2):1962–74. doi:10.1109/tsg.2024.3503554.
9. Kilthau M, Henkel V, Wagner LP, Gehlhoff F, Fay A. A decentralized optimization approach for scalable agent-based energy dispatch and congestion management. Appl Energy. 2025;377:124606. doi:10.2139/ssrn.4743101.
10. Al-Shamma'a AA, Farh HMH, Taiwo R, Ibrahim AW, Alshaabani A, Mekhilef S, et al. A comprehensive review of sizing and allocation of distributed power generation: optimization techniques, global insights, and smart grid implications. Comput Model Eng Sci. 2025;145(2):1303–47. doi:10.32604/cmes.2025.071302.
11. Wei H, Ma M, Jiang H, Capuder T, Teng F, Strbac G, et al. Generation and transmission expansion planning incorporating economically feasible heterogeneous demand-side resources. Appl Energy. 2025;381:125067. doi:10.1016/j.apenergy.2024.125067.
12. Yuwono B, Kranzl L, Haas R, Dewi RG, Siagian UWR, Kraxner F, et al. Incorporating grid development in capacity expansion optimisation: a case study for Indonesia. Appl Energy. 2025;378:124837. doi:10.1016/j.apenergy.2024.124837.
13. Xiong Z, Shen X, Sun H. Two-stage robust planning for park-level integrated energy system considering uncertain equipment contingency. IEEE Trans. Smart Grid. 2025;16(2):1112–26. doi:10.1109/tsg.2024.3524879.
14. He C, Hu Z, Liu X, Nan L, Liu T. Coordinated expansion planning of integrated electricity and natural gas distribution systems for enhancing both inherent and dynamic resilience: a distributionally robust approach considering decision-dependent uncertainty. Energy. 2025;333:137378. doi:10.1016/j.energy.2025.137681.
15. Zhang J, Chang X, Xue Y, Bai X, Li Z, Wang P, et al. Optimal planning for electricity-gas–hydrogen integrated energy systems considering intertemporal long-term hydrogen storage and multiple uncertainties. IEEE Trans Power Syst. 2025;40(6):4660–74. doi:10.1109/tpwrs.2025.3577703.

16. Liu Y, Chen Y, Xin H, Tu J, Zhang L, Song M, et al. System strength constrained grid-forming energy storage planning in renewable power systems. IEEE Trans Sustain Energy. 2025;16(2):981–94. doi:10.1109/tste.2024.3494259.
17. Ding X, Du Y, Shen X, Wu Q, Zhang X, Hatziargyriou ND. Reliability-based planning of cable layout for offshore wind farm electrical collector system considering post-fault network reconfiguration. IEEE Trans Sustain Energy. 2025;16(1):419–33. doi:10.1109/tste.2024.3462476.
18. Du Y, Shen X, Lu B, Ding X. Joint optimization of layout and electrolyzer capacity for decentralized offshore wind-powered hydrogen production. IEEE Trans Ind Inform. 2025;21(5):4158–68. doi:10.1109/tii.2025.3538067.
19. Lu B, Shen X, Du Y, Huang Z, Tan R. Offshore wind farm micro-siting based on two-phase hybrid optimization. Appl Energy. 2025;381:125105. doi:10.1016/j.apenergy.2024.125105.
20. Hrgović I, Pavić I. Sizing and implementation of phase-shifting transformer for congestion management in renewable-rich regions: a case study of the croatian power grid. IEEE Trans Power Syst. 2025;40(4):3465–73. doi:10.1109/tpwrs.2025.3526264.
21. El-Ela AAA, El-Sehiemy RA, Nazih A, Mubarak AA, Ali ES. A review of modern strategies for enhancing power quality and hosting capacity in renewable-integrated grids: from conventional devices to AI-based solutions. Comput Model Eng Sci. 2025;145(2):1349–88. doi:10.32604/cmes.2025.069507.
22. Wu H, Kong Q, Huber M, Sun M, Craig MT. Climate change will increase high-temperature risks, degradation, and costs of rooftop photovoltaics globally. Joule. 2026;10(1):102218. doi:10.21203/rs.3.rs-6605168/v1.
23. Ding B, Li Z, Li Z, Xue Y, Chang X, Su J, et al. Cooperative operation for multiagent energy systems integrated with wind, hydrogen, and buildings: an asymmetric nash bargaining approach. IEEE Trans Ind Inform. 2025;21(8):6410–21. doi:10.1109/tii.2025.3563589.
24. Taleb I, Guerard G, Fauberteau F, Nguyen N, Clain P. A flexible decision method for holonic smart grids. Comput Model Eng Sci. 2025;145(1):597–619. doi:10.32604/cmes.2025.070517.
25. Zhao C, Zhou M, Li J, Fu Z, Liu D, Wu Z. Evolutionary pathways of renewable power system considering low-carbon policies: an agent-based modelling approach. Renew Energy. 2025;244(1):122686. doi:10.1016/j.renene.2025.122686.
26. Wu H, Qiu D, Zhang L, Sun M. Adaptive multi-agent reinforcement learning for flexible resource management in a virtual power plant with dynamic participating multi-energy buildings. Appl Energy. 2024;374:123998. doi:10.1016/j.apenergy.2024.123998.
27. Xiong K, Wei Q, Liu Y. Community microgrid energy co-scheduling based on deep reinforcement learning and contribution mechanisms. IEEE Trans. Smart Grid. 2025;16(2):1051–61. doi:10.1109/tsg.2024.3461320.
28. Zhao Y, Liu T, Hill DJ. Distributed attention-enabled multi-agent reinforcement learning based frequency regulation of power systems. IEEE Trans. Power Syst. 2025;40(3):2427–37. doi:10.1109/tpwrs.2024.3469132.
29. Du S, Ding T, Xiao Y, Wan J, Liu J, Meng F. Real-time scheduling of high-penetrated renewable power systems: an expert knowledge and reinforcement learning hybrid approach. IEEE Trans Power Syst. 2025;40(2):1545–57. doi:10.1109/tpwrs.2024.3423381.
30. Guan Y, Ma W, Che L, Shahidehpour M. Model-based safe reinforcement learning for active distribution network scheduling. IEEE Trans. Smart Grid. 2025;16(3):2375–88. doi:10.1109/tsg.2025.3547843.
31. Zhang H, Sun X, Lee MH, Moon J. Deep reinforcement learning-based active network management and emergency load-shedding control for power systems. IEEE Trans Smart Grid. 2024;15(2):1423–37. doi:10.1109/tsg.2023.3302846.
32. Sun X, Peng C, Jia X, Zhang Y. Brain-inspired deep reinforcement learning for load frequency control of power systems with composite interference. IEEE Trans Ind Inform. 2025;21(7):5182–90. doi:10.1109/tii.2025.3552697.
33. Xia T, Zhang N, Li W, Du E, Su Y, Fang C, et al. Efficient embedding of neural network-based stability constraints into power system dispatch. IEEE Trans. Power Syst. 2024;39(3):5443–6. doi:10.1109/tpwrs.2024.3363948.
34. Eichelbeck M, Markgraf H, Althoff M. Commonpower: a framework for safe data-driven smart grid control. IEEE Trans Smart Grid. 2026;17(1):71–82. doi:10.1109/tsg.2025.3616402.

35. Lei C, Bu S, Wang Q, Chen Q, Yang L, Chi Y. Look-ahead rolling economic dispatch approach for wind-thermal-bundled power system considering dynamic ramping and flexible load transfer strategy. IEEE Trans Power Syst. 2024;39(1):186–202. doi:10.1109/tpwrs.2023.3238035.
36. Qiu J, Zhao J, Wen F, Zhao J, Gao C, Zhou Y, et al. Challenges and pathways of low-carbon oriented energy transition and power system planning strategy: a review. IEEE Trans Netw Sci Eng. 2024;11(6):5396–416. doi:10.1109/tnse.2023.3344729.
37. Ghanbarzadeh T, Habibi D, Aziz A. Addressing reliability challenges in generation capacity planning under high penetration of renewable energy resources and storage solutions: a review. Renew Sustain Energ Rev. 2025;212:115461. doi:10.1016/j.rser.2025.115461.
38. Yang B, Zhou Y, Yan Y, Su S, Li J, Yao W, et al. A critical and comprehensive handbook for game theory applications on new power systems: structure, methodology, and challenges. Prot Control Mod Power Syst. 2025;10(5):1–27. doi:10.23919/pcmp.2024.000297.
39. Seguro JV, Lambert TW. Modern estimation of the parameters of the weibull wind speed distribution for wind energy analysis. J Wind Eng Ind Aerodyn. 2000;85(1):75–84. doi:10.1016/s0167-6105(99)00122-1.
40. Saint-Drenan YM, Besseau R, Jansen M, Staffell I, Troccoli A, Dubus L, et al. A parametric model for wind turbine power curves incorporating environmental conditions. Renew Energy. 2020;157:754–68. doi:10.1016/j.renene.2020.04.123.
41. Youcef Ettoumi F, Mefti A, Adane A, Bouroubi MY. Statistical analysis of solar measurements in algeria using beta distributions. Renew Energy. 2002;26(1):47–67. doi:10.1016/s0960-1481(01)00100-8.
42. Al-Sumaiti AS, Ahmed MH, Rivera S, El Moursi MS, Salama MMA, Alsumaiti T. Stochastic PV model for power system planning applications. IET Renew Power Gener. 2019;13(16):3168–79. doi:10.1049/iet-rpg.2019.0345.
43. Carrión M, Arroyo JM. A computationally efficient mixed-integer linear formulation for the thermal unit commitment problem. IEEE Trans Power Syst. 2006;21(3):1371–8. doi:10.1109/tpwrs.2006.876672.
44. Gafurov T, Usaola J, Prodanovic M. Modelling of concentrating solar power plant for power system reliability studies. IET Renew Power Gener. 2015;9(2):120–30. doi:10.1049/iet-rpg.2013.0377.
45. Yu Q, Li X, Wang Z, Zhang Q. Modeling and dynamic simulation of thermal energy storage system for concentrating solar power plant. Energy. 2020;198:117183. doi:10.1016/j.energy.2020.117183.
46. Chen H, Zhuang K, Wang Z, Xue J, Li Y. A transmission network planning method based on particle swarm optimization. In: Proceedings of the 2024 3rd International Conference on Energy, Power and Electrical Technology (ICEPET); 2024 May 17–19; Chengdu, China. p. 768–71.
47. Li Y, Wu F. Multistrategy fusion particle swarm for dynamic economic dispatch optimization of renewable energy sources. Int J Energy Res. 2024;2024:5992081. doi:10.1155/2024/5992081.